Ultrasonics 99 (2019) 105956

Contents lists available at ScienceDirect

Ultrasonics

journal homepage: www.elsevier.com/locate/ultras

CMUT-based biosensor with convolutional neural network signal processing

Donatas Pelenis[a,b], Dovydas Barauskas[a], Gailius Vanagas[a], Mindaugas Dzikaras[a], Darius Viržonis[a,*]

[a] Kaunas University of Technology, Panevėžys Faculty, Panevėžys, LT 37164, Lithuania
[b] Panevėžys Mechatronic Center, Panevėžys, LT 36239, Lithuania

ARTICLE INFO

Keywords:
Biosensors
CMUT
CNN
Signal processing

ABSTRACT

The improvement of the micromachined ultrasound transducer based (CMUT) biosensor fabrication technology and signal processing, which led to higher signal to noise ratio is reported. The biosensor contains interdigitally arranged CMUT structure with gold-coated analytical area. It is assembled with the plexiglass microchannels. CMUTs were fabricated with the wafer bonding technology for 5 MHz operation in immersion. For signal processing the convolutional neural network (CNN) was developed and trained to classify the sensor data to different propagation delay values. For training of the network 750 thousand signals representing different properties of the bioanalyte and different noise conditions was simulated by the finite time difference domain (FDTD) model. The capability of the CNN algorithm to classify the propagation delay data was compared with the adaptive passband filter signal processing algorithm used in our previous version of the senor. Both sensing channels were run simultaneously with the reference liquids in the microchannel: deionized water switching to 0.9% saline. It was found that CNN channel is capable to improve the signal to noise ratio for this experiment to 75 dB, when the same property for the passband filter channel was only 60 dB. This led to the generalization about the advantage of CNN channel to provide 15 dB less of instrumental noise. Finally, the real-time detection ability of the bovine serum albumin (BSA) deposition on the analytical area of improved sensor was demonstrated.

1. Introduction

Biosensors are currently on the agenda of the developers of innovative and personalized medical care. World scientists and technology companies devote a lot of effort and resources to the development of low-cost biosensor technology, and significant part of that is related to the biosensing techniques based on microelectromechanical (MEMS) structures [2–9]. An extensive survey of innovative technologies and applications of the acoustically operated biosensors was recently made by Fogel et al. [1].

Development of any type of a biosensor faces challenges in parameterization and calibration. Usually, when carrying out these steps, it is necessary to perform a large number of experimental studies and to find the signal processing methods, which would be flexible enough to capture the actual biological interaction with as low noise and measurement errors as possible [2]. Biological elements, which are often used to functionalize the biosensors, are less stable than functionalization materials commonly used for other types of the sensors, for example, gas and chemical sensors [3]. Also, in contrast to the chemical sensing, biosensors are subject to certain incubation period, during which unmeasured and uncontrolled changes in the operation conditions due to the side reactions, protein denaturation and other effects are to be accounted for [4]. Therefore, flexibility and adaptivity of the signal processing algorithms is a must-have in biosensors.

One of the emerging types of the biosensors is based on microelectromechanical detection of the analyte mass and other physical properties by using the capacitive micromachined ultrasonic transducers (CMUT). In our earlier research we have shown CMUT structure to have a good potential for real-time biosensing [5] also in the liquid phase if designed to have the interdigital transducer (IDT) setup of the acoustic excitation and sensing elements integrated within the microchannel [3]. It was shown that bioanalytes can be detected by the transverse Scholte type waves propagating along the microchannel at the fluid – liquid interface [5]. This biosensor setup was demonstrated by our group to be suitable for real-time detection of the bovine serum albumin (BSA) deposition within the microchannel by measuring the propagation delay of the acoustic pulse [6]. Since previously we used only the basic algorithms to detect the envelope of the received pulse,

* Corresponding author.
E-mail addresses: donatas.pelenis@ktu.edu, donatas@panmc.lt (D. Pelenis), darius.virzonis@ktu.lt (D. Viržonis).

https://doi.org/10.1016/j.ultras.2019.105956
Received 29 April 2019; Received in revised form 29 June 2019; Accepted 29 June 2019
Available online 02 July 2019
0041-624X/

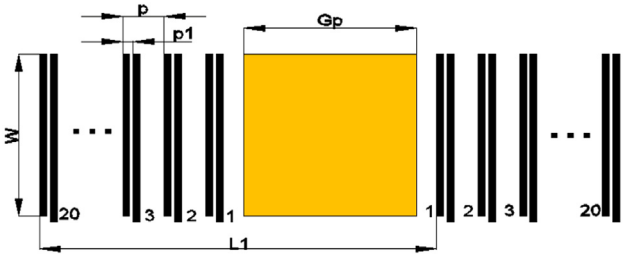

Fig. 1. The layout of the cMUT biosensor.

early version of the sensor had comparatively low signal to noise ratio [7].

In the present research we demonstrate a significant increase of the signal to noise ratio while using trained convolution neural network for the propagation delay measurement. We believe that a trained convolutional neural network has superior noise resistance potential when compared to other known methods of acoustic wave propagation delay and/or attenuation measurements in the context of biosensing.

For the experiments we used CMUT devices, which were similarly structured as in our previous work, but the structures were fabricated by the wafer bonding technology instead of the sacrificial release technique [6,8] and therefore had improved technical properties.

2. Methods

2.1. Design and fabrication of CMUT biosensor devices

The layout of the CMUT IDTs pair is shown in Fig. 1, where p is the IDT period ("pitch") and W is the finger length or the aperture width. Unlike the piezoelectric IDTs, where a pair of the surface electrodes establish one finger of the transducer, CMUT interdigital transducers need only one surface electrode, since another one is at the bottom of the device (Fig. 2). So, we used the opportunity to have the double finger setup, which enabled the sensor to have directional wave excitation and receiving capabilities.

The microstructure of the interdigital CMUT (shown in the Fig. 1) was designed for 5 MHz resonance when immersed in water. The pitch between the finger pairs $p = 300$ µm, which is equal to the wavelength of the Scholte wave excited at 5 MHz and propagating between the silicon and water interface with 1481 m/s phase velocity [9]. This allows placing two sub-fingers within $p1 = \lambda/4$ wavelength to enable the control over directionality of the IDT by introducing the 90° phase difference between the finger pair. Both IDTs have the same number of finger pairs (20). In the middle of the CMUT biosensor there is an analyte-binding area, coated with a 100 nm thick gold film for improved adhesion and interaction of the biological elements. The

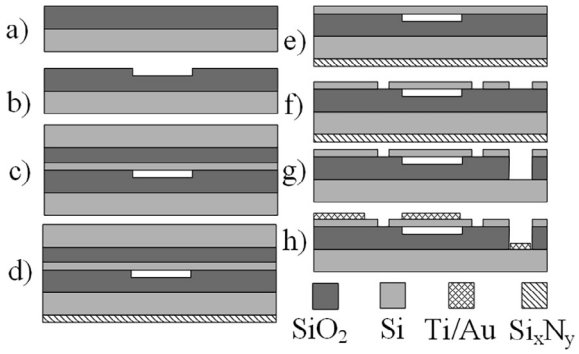

Fig. 2. Main CMUT fabrication steps: (a) thermal oxidation; (b) oxide wet etch; (c) wafer bonding; (d) backside protection with PECVD silicon nitride; (e) handle wafer removal; (f) device layer etch and separation of devices; (g) opening of the bottom electrode, (h) top electrode and contact pads deposition.

distance between the transmitter and the receiver (edge-to-edge or center-to-center) L1 = 14.7 mm, the length of the analyte-binding square area for biological interaction is Gp = 10 mm. The aperture width W = 3 mm.

As shown in the earlier research [3,6,22], interdigitally arranged CMUT structure is capable to excite and receive the Scholte type waves, which are propagating at the solid and liquid interface and are considered to be informative when detecting the biochemical interaction on the surface of the analytical area of the sensor.

The microstructure of a CMUT cell and main fabrication steps are schematically shown in the Fig. 2. Initially, highly doped silicon wafers (less than 0.01 Ωcm) were oxidized in an oxidation furnace resulting with 300 nm of the thermally grown oxide layer (Fig. 2a). Then, by UV photolithography and buffered oxide etch, the pattern of the vacuum cavities was defined (Fig. 2b). Wafers with the cavities were fusion bonded to the silicon on insulator (SOI) wafers with a device layer thickness of 2.5 µm, thus forming sealed CMUT structures (Fig. 2c). In this case, the membrane thickness was determined by the device layer of the SOI wafer. The backside of the background wafer was protected by depositing PECVD silicon nitride (Fig. 2d). Membranes were released by removing the SOI handle wafer (Fig. 2e). After release, next lithography patterning step and subsequent Oxford process was used to etch through the device layer to electrically and mechanically separate structures (Fig. 2f). Another UV photolithography step was taken to define the top CMUT electrodes and bonding pads (Fig. 2g). Finally, the passivation layer of low-stress plasma enhanced silicon nitride film (200 nm) was deposited for electrical isolation of the electrodes from the environment (Fig. 2h). Fabricated devices after a dicing step were assembled with the custom-made printed circuit boards. The contact pads of CMUT devices were directly wire bonded to the PCB leads.

After fabrication and wire bonding steps all devices were tested and characterized in air using Agilent 4395A network analyzer with an impedance measurement kit and a DC voltage supply.

2.2. Finite difference time domain model of transverse acoustic waves within the sensor structure

Finite difference time domain (FDTD) method is often used for numerical simulations of waves propagation in the time domain [10]. The main advantage of this method is its comparative simplicity of implementation and ability to cover a wide range of physical domains, including electromagnetism, ultrasound and acoustics [11]. This modeling method was used for modeling of transverse, Scholte-type waves propagating along the solid and liquid interface [12]. The k-Wave toolbox MATLAB add-on, which features two-dimensional FDTD simulation of elastic waves capabilities was chosen and modified according to the task [11]. The computation is based on a pseudo spectral time-domain model which accounts for viscoelastic absorption and heterogeneous material parameters.

In our model the elastic wave propagation is governed by the equation of motion and the elastic equation. These equations can be written as a first-order differential equation system for the components of stress ($\sigma_{i,i}$, $\sigma_{i,j}$, $\sigma_{j,j}$) and particle velocity (v_x , v_z) [6,7]:

$$\frac{\partial v_x}{\partial t} = \frac{1}{\rho}\left(\frac{\partial \sigma_{i,i}}{\partial x} + \frac{\partial \sigma_{i,j}}{\partial z}\right) \quad (1)$$

$$\frac{\partial v_z}{\partial t} = \frac{1}{\rho}\left(\frac{\partial \sigma_{i,j}}{\partial x} + \frac{\partial \sigma_{j,j}}{\partial z}\right) \quad (2)$$

$$\frac{\partial \sigma_{i,i}}{\partial t} = (\lambda_L + 2\mu)\left(\frac{\partial v_i}{\partial x} + \frac{\partial v_j}{\partial z}\right) \quad (3)$$

$$\frac{\partial \sigma_{j,j}}{\partial t} = (\lambda_L + 2\mu)\left(\frac{\partial v_j}{\partial z} + \frac{\partial v_i}{\partial x}\right) \quad (4)$$

$$\frac{\partial \sigma_{i,j}}{\partial t} = \mu\left(\frac{\partial v_j}{\partial z} + \frac{\partial v_i}{\partial x}\right) \tag{5}$$

The wave propagation is governed by the Kelvin-Voigt equation:

$$\frac{\partial \sigma_{ij}}{\partial t} = \lambda_L \delta_{ij} \frac{\partial v_k}{\partial x_k} + \mu\left(\frac{\partial v_i}{\partial x_j} + \frac{\partial v_j}{\partial x_i}\right) + \chi\delta_{ij}\frac{\partial^2 v_k}{\partial x_k \partial t} + \eta\left(\frac{\partial^2 v_i}{\partial x_j \partial t} + \frac{\partial^2 v_j}{\partial x_i \partial t}\right) \tag{6}$$

Here $\sigma_{i,j}$ is the stress tensor, λ_L and μ are the Lame parameters, where λ_L is elastic modulus, μ is the shear modulus, and χ and η are the longitudinal and transverse viscosity coefficients, correspondingly. To represent the interaction of the solid and liquid media, the model must account for the continuity of the particle displacement and balance the pressure transfer between the both media and energy dissipation within the liquid and solid. Instead of explicitly satisfying the boundary conditions, we used effective medium parameters, because they provide a more adequate representation of the physical properties by appropriately satisfying the energy transfer continuity across the interface. Effective shear modulus will decrease during the wave propagation due the losses, when the energy is passed between the solid and liquid [10]. This can be described as follows:

$$\mu^{i+\frac{1}{2},j+\frac{1}{2}} = \frac{1}{\left[\frac{1}{4}\left(\frac{1}{\mu^{i,j}} + \frac{1}{\mu^{i+1,j}} + \frac{1}{\mu^{i,j+1}} + \frac{1}{\mu^{i+1,j+1}}\right)\right]}. \tag{7}$$

The mass densities of solid and liquid average over the solid-fluid interface:

$$\rho^{i+\frac{1}{2},j} = \frac{1}{2}(\rho^{i,j} + \rho^{i+1,j}); \tag{8}$$

$$\rho^{i,j+\frac{1}{2}} = \frac{1}{2}(\rho^{i,j} + \rho^{i,j+1}); \tag{9}$$

Calculation of the boundary condition of the shear modulus as the energy is traveling from solid to fluid medium (Eq. (7)) ensures that shear stresses vanish across the fluid-solid interface. A solid-fluid element representing the interface between the both media is shown graphically in the Fig. 3.

The model structure is established by two homogeneous layers (Fig. 3). The upper layer is a fluid half-space, and the lower half-space is an isotropic solid. For most of the biodetection in liquid situations it is adequate that the fluid density is between 800 kg/m^3 and 1100 kg/m^3, the speed of sound in the fluid is between 1100 m/s and 1600 m/s. The solid density is 2330 kg/m^3 (which corresponds to the monocrystalline silicon), the longitudinal wave speed is 8412 m/s, and the transverse wave speed is 5078 m/s. Measured and simulated sensor readings are shown in the Fig. 4. In the frequency domain representation of the measured signal, one can identify two peaks at 4.8 MHz and 5.2 MHz, whereas in the simulated signal there is only a single peak at 5.2 MHz. We attribute the missing peak at 4.8 MHz to the guided mode of the ultrasonic waves, which is propagating due to the reflections from the microchannel walls. The evidence for this is strong relationship between the parameters of this mode and microchannel dimensions. This effect is not captured by the model since the model was designed only to simulate the Scholte type wave propagation at the interface between the solid and liquid, not the guided waves.

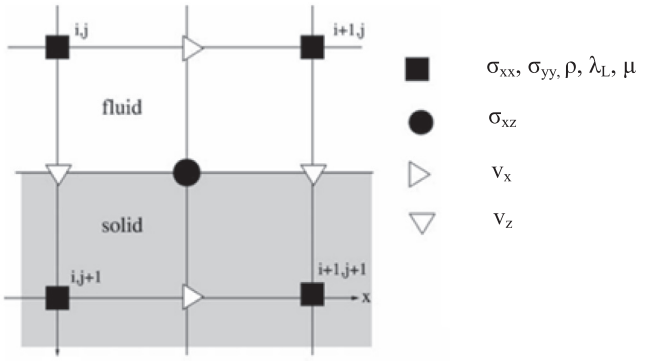

Fig. 3. An FDTD element representing the solid – fluid interface [12].

2.3. Building and using spectrograms for neural network training and operation

In order to make the training and operation of the neural network more effective, time domain sensor signals are converted to the frequency domain signals and then combined to two-dimensional time-frequency domain arrays. The fast Fourier transform is used to extract the signal frequency spectra since it is easy to implement and scale. Sampling of the frequency spectra is synchronized with a single transmit – receive cycle, so each received pulse, framed by the 20 μs long time window, is converted to the frequency domain. Then spectra of 916 received pulses with 60 data points each are combined to 60 by 916 spectrogram array. Thus, each spectrogram array covers 20 μs sampling period.

To train the neural network we needed large amount of representative data, which were generated by simulation of the time-domain signals as described in the subchapter 2.2. In order to have adequate noise resistance of the trained network, simulated signals were added with the white noise and flicker noise with a signal to noise ratio from 0 to 30 dB. Each simulated sample was scaled up to 500 different cases of noisy signals. Also, simulation parameters were changed to cover different damping, speed of sound and propagation delay scenarios. In total, over 750 thousand spectrogram samples, associated with different propagation delay values were used to train the neural network (see also Fig. 7).

2.4. Data processing for the propagation delay measurement without the CNN

The following data processing method was used in our earlier works [6,8] and is shortly described here since we used it to have results for comparison with the CNN method. For noise elimination we used an adaptive infinite impulse response band pass filter (band-pass IIR) applied on the received signal. After the capturing of each receive impulse, the data were converted to the frequency domain, and the central frequency f of the signal was used to adjust the filter band [$f1$; $f2$], where $f1 = f - 800$ kHz and $f2 = f + 800$ kHz. After filtering, the appearance time of the maximum of the received pulse envelope peak (see the “Tracked node” marker in Fig. 5) in the time domain was read and then used to calculate the propagation delay.

2.5. Neural network architecture and training

Convolutional neural networks (CNN) are commonly used for data processing, interpretation of the natural language, computer vision and usually are described by a grid type topology. The convolutional neural network, like the name suggests, is using at least one mathematical operation known as convolution during the training phase. The CNN is using data weights, thus reducing the number of parameters that CNN needs to learn from the data, as well as reducing training time and resources used to train the neural network [13].

The overall CNN architecture used in the present work is shown in the Fig. 6. For learning we used traditional ConvNet architecture [INPUT– CONV – RELU – POOL – CONV – RELU – POOL – FC]. INPUT [60 × 916 × 1] holds the weight values of the spectrogram. Convolution layer computes the output of the neurons that are connected to the local regions of the input, each computing a dot product between their weights and a small region they are connected to in the input volume. This results in volume such as [60x916x10] if 10 filter layers are used. Rectified linear unit layer (RELU) will apply activation function, such as the max(0,x) thresholding at zero. This leaves the size of the volume

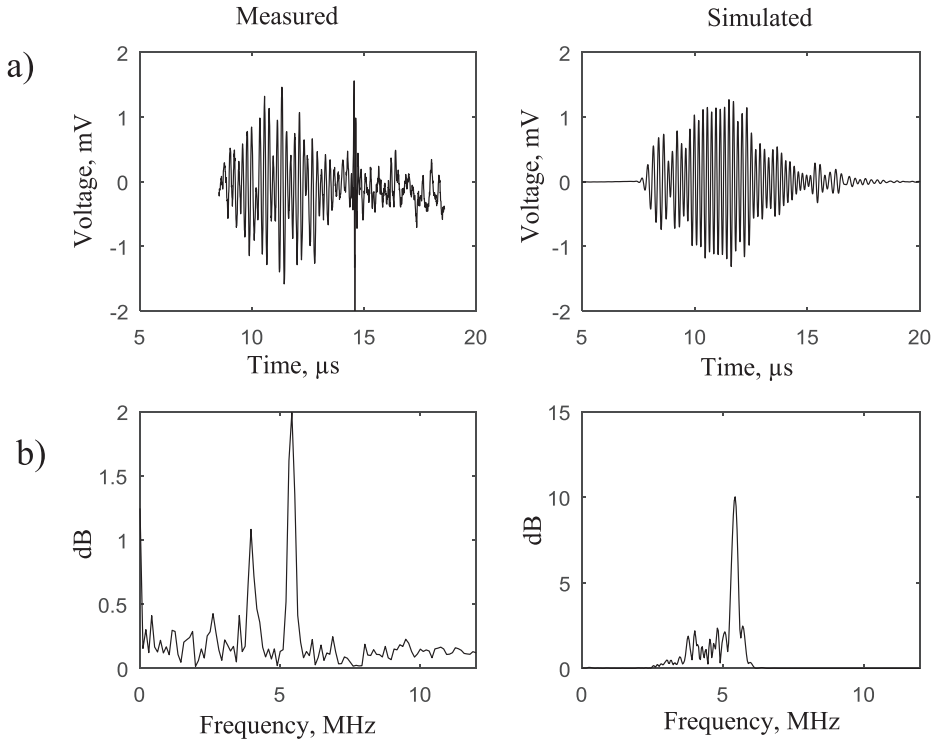

Fig. 4. Verification of the FDTD model: (a) measured and simulated time domain signals; (b) simulated and measured signals after conversion to the frequency domain.

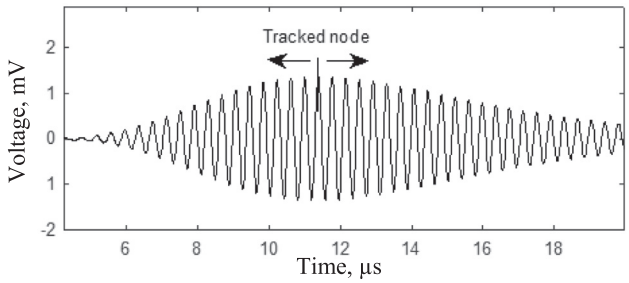

Fig. 5. Propagation delay detection in received pulse after band-pass IIR filtering.

unchanged ([60x916x10]). Downsampling operations are performed using POOL layer along the spatial dimensions (width, height), resulting in volume such as [30 × 158 × 10]. In the next step, CONV [30 × 158 × 20], RELU[30 × 158 × 20], and POOL[15 × 79 × 20] are used again. Two-stage layers extract the useful features from the spectrogram, introduce non-linearity in our network and reduce feature dimension while aiming to make the features somewhat equivariant to scale and translation. The Fully Connected layer (FC) computes the class scores, resulting in a volume of size [1x150], where each of the 150 numbers corresponds to a class score, such as among the 150 categories modeling propagation delay [13–19].

The CNN was trained using the Stochastic Gradient Descent with Momentum (SGDM) using backpropagation with 20 epochs. The learning rate was set to $1{\cdot}10^{-4}$, and the cross-entropy loss function was used. For training we used the groups of spectrograms generated as described before. In order to monitor the generalization performance and to select the best training model, we have defined the validation dataset consisting of 20% simulated data, which were not used during the training, 5% of measured signals and 75% of signals used for the network training. Overall workflow of the training and validation database development is illustrated in the Fig. 7. To implement and train the CNN we have used the MATLAB parallel computing framework.

3. Experimental testing of the biosensor

The setup of the experimental system is shown in Fig. 8. The sensor

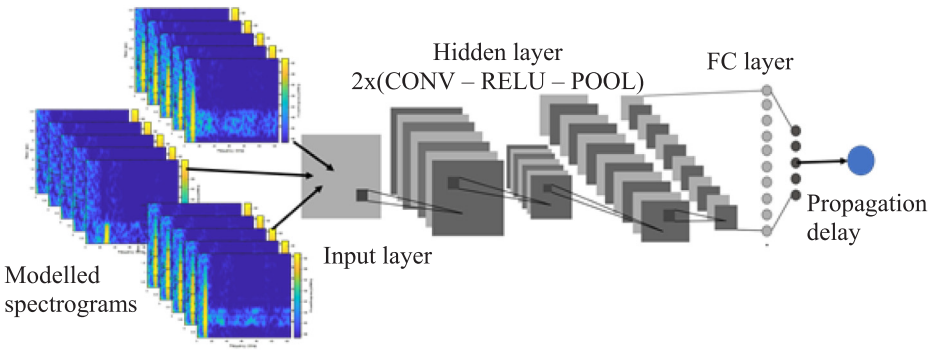

Fig. 6. CNN architecture for the propagation delay classification.

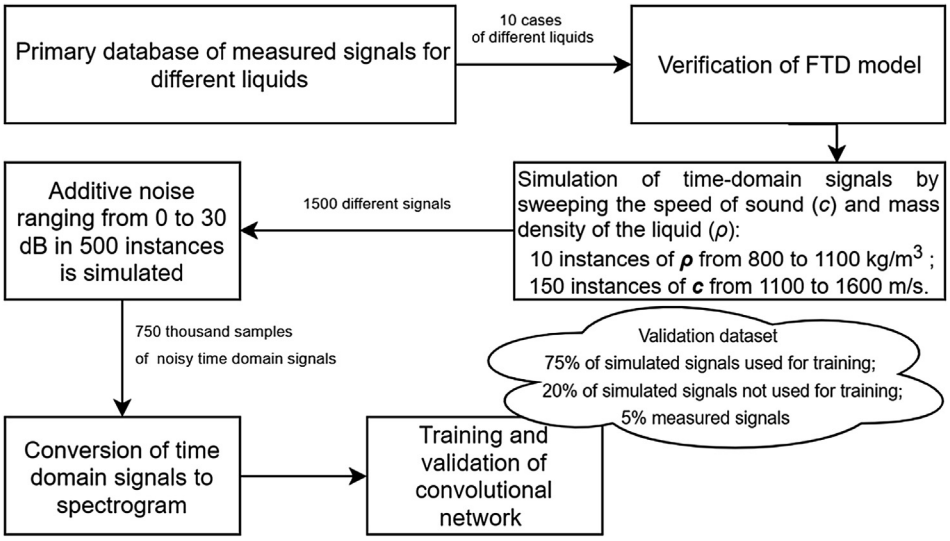

Fig. 7. The flowchart of the development of the database for the training of the convolutional network.

with CMUT IDTs (1) is integrated with the microchannel. The microchannel is made of plexiglass with two 0.3 mm thick fluid introduction and output ports on its sides. The plexiglass was attached to the CMUT chip by using 100 μm thick kapton film spacer, thus establishing the microchannel with dimensions of 20 mm × 3 mm × 100 μm. During our sensing tests, one of the CMUT IDTs was connected to the two-phase transmitter (composed of two-phase arbitrary waveform generator 3, Agilent 33522A); the second IDT was connected to the receiver of transmit/receive switch (6, TX810), a low noise amplifier (7, LNA-AD8432) and an oscilloscope (8, Fluke 190-502/AM). The bias source (5, Agilent N5752A) is common for both IDTs and is applied via the bias-T (4). There is also the synchronization link between the transmitter and receiver, which is not shown in the Fig. 7. We also monitored the temperature of the liquid at the output of the microchannel by an immersed thermocouple to detect possible correlation between the temperature change and the change of the propagation delay.

We performed two experiments with the described sensor experimental testing setup. The purpose of the first experiment was to validate experimentally the trained CNN and compare the signal to noise ratio with an earlier signal processing algorithm as described in the subchapter 2.4. During this experiment, we used reference liquids (deionized water and saline) as the media with known densities, sound speeds and attenuation factors to fill the microchannel. Reference parameters of the liquids are shown in the Table 1. During the experiment, we switched the microchannel input between the fluids without interruption of the data acquisition. For estimation of the signal to noise ratio we used the mathematical reference obtained from the noise-free FDTD model.

In the second experiment we demonstrated the biosensing operation of the trained CNN. For biosensing ability demonstration, we introduced into the microchannel 0.1 mg/mL, 1 mg/mL and 3 mg/mL of bovine serum albumin (BSA) solution. Dynamics of BSA deposition from the solution in the presence of the gold thin film surface are well described in many biochemical experiments and in our earlier publication [20].

4. Results

4.1. Testing the trained CNN

In the Fig. 9 the signal processing by the trained CNN is illustrated. The left image shows an example of the original received pulse, the central image shows the spectrogram sampled over 20 μs period, and the classification error map is shown on the right. From the classification error map one can see comparatively even distribution of the classification errors over the spectrogram. This suggests that filtering of the noise even with the narrow band-pass filter can be ineffective.

Characteristic parameters of the liquids used for trained CNN validation are shown in the Table 1. Measurements were taken in a controlled temperature environment, since speed of sound in water and water-based solutions, like saline, is sensitive to the temperature. The temperature of the liquids was kept at 20 °C. Table 1 also shows the percentage of the liquid identification errors both for simulated and measured signals. Comparatively high error rate (up to 11.4%) for the

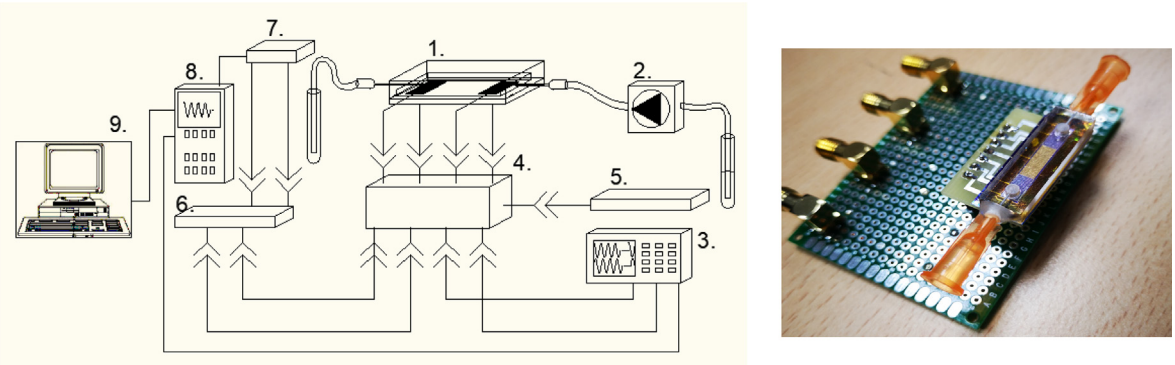

Fig. 8. Left: 1 – SAW biosensor; 2 – Peristaltic pump; 3 – Signal generator; 4 – AC + DC; 5 – DC supply; 6 – T/R Switch; 7 – LNA; 8 – 2 CH oscilloscope; 9 – PC; right: fully assembled biosensor.

Table 1
Results of trained CNN operation.

Material	The speed of sound in the fluid, m/s	Density, kg/m3	Simulated data, errors (%)	Measured data errors (%)
Deionized water (20 °C)	1481	997	1.5	9.1
Sodium chloride, 0.9% solution ('saline', 20 °C)	1450	1040	1.8	11.4

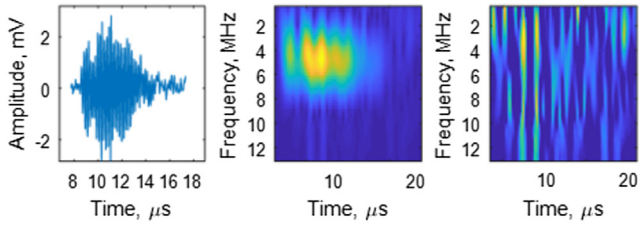

Fig. 9. Signal processing by a CNN. Left image shows original time-domain signal, the center image shows the spectrogram of the measured signal over 20 μs sampling period and the right image shows the error map of the CNN operation.

saline experiments is probably related to the higher damping of the signal, which is mainly due the poor wetting of the silicon nitride by the saline liquid. Also, the error rate for experimental data is somewhat higher than for simulated, because during the real-time data processing by CNN, some unrecognized noise occurred, especially during switching between the liquids, when air microbubbles were trapped in the tubing and microchannel.

4.2. Results of the sensing experiments

As mentioned before, real-time sensing experiments were carried out to discover the practical advantage of CNN approach for the sensor signal processing. In the first experiment, we compared the passband filtering method from our earlier work and CNN classification algorithm with the output of the noise-free FDTD model. Simultaneous propagation delay readings of both signal processing channels during the step change of the liquid in the microchannel are shown in the Fig. 10. The lowermost line shows the readings obtained from the CNN channel, and the uppermost line shows the output of the passband filtering channel. The middle line is a mathematical reference obtained from the noise-free FDTD model. The experiment started by pumping the deionized water through the microchannel at 0.4 cm^3/min debit. Approximately at 100th second of the experiment the input line of the microchannel was switched to a container with saline. The readings of both channels as for as the reference line initially show the plateau

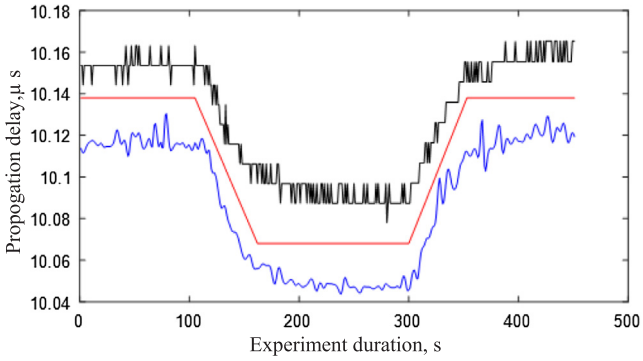

Fig. 10. Real-time time-of-flight readings during switching between DI water and 0.9% saline. Lines are shifted in vertical scale by 20 ns from the mathematical reference for better visual perception. The middle line shows mathematical reference of the process; the uppermost line shows the readings of the passband filtering channel; the bottom line represents the output of the CNN channel.

during the first 100 s, followed by decreasing propagation delay after switching the liquids and stabilizing again to the plateau after next 100 s. After 300th second of the experiment the input of the microchannel was switched again to the deionized water. This caused the propagation delay readings to regain an initial value after approximately 100 s of stabilization.

Comparing the readings of both channels with the mathematical reference one can see some higher frequency fluctuations of the readings present in each of them. We attribute these fluctuations as an instrumental noise, which manifests itself differently in each channel. Propagation delay measurement resolution of the passband filtering channel is limited by the sampling period of the original signal, which is 9 ns. This causes fluctuations in this channel to have quantified character. As a contrast, no quantification limit in the resolution of the CNN channel exist, so the distribution of the amplitudes of the fluctuations are much more even. After elimination of the dynamic effects related to the microfluidic system and referring to the mathematical reference, we estimated the signal to noise ratio to be 60 dB for the passband filtering channel and 75 dB for the CNN channel in the saline experiment. This results in an improvement of the signal to noise ratio by 15 dB of the CNN algorithm as compared to the passband algorithm.

Our second sensing experiment consisted of sensing of BSA deposition on the sensor analytical area. It is widely known, that BSA tend to form an even monolayer over the gold surface [21], which makes it suitable to model the protein deposition within the biosensor structure. Fig. 11 depicts the BSA deposition sensing data in the experiment with aqueous solutions of different BSA concentrations. The solutions were prepared by dissolving the dry BSA powder (purchased from Sigma Aldrich) in corresponding volume of deionized water right before the experiment. This time we used solely the CNN signal processing and additional smoothing filter to exclude instrumental noise. The experiment started by supplying the microchannel of the sensor with the deionized water, which was switched to various BSA solutions after initial 300 s. Then, after BSA deposition period, which lasted up to 2500 s, microchannel input was switched back to the deionized water. The pulse shown by the dashed line shows the period of exposing the sensor to the BSA solutions. For each measurement a fresh sensor (not contaminated previously with BSA) was used to have the same propagation delay reference point to start from.

It can be seen from the diagrams shown in the Fig. 10 that different BSA concentrations cause different dynamics of the sensor readings. After switching to the BSA solution, decrease of the propagation delay

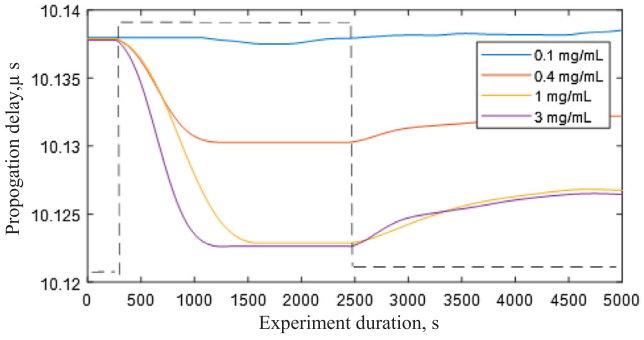

Fig. 11. Sensing of BSA deposition from aqueous solutions of different concentrations. The dashed line shows the period at which the sensor was exposed to the BSA solutions.

readings can be observed in all cases. Initial decrease of the propagation delay is related to the dynamics of propagation of the solution through the microchannel and deposition of BSA on the analytical area of the sensor. Then the slope of the readings for all BSA concentrations (except of 0.1 mg/mL case) turns to the plateau, and after switching back to the deionized water tend to increase and stabilize at the level, which is different from the initial reference point. While the sensor is exposed to the BSA solution, propagation delay readings are reflecting the effect of increased density of the liquid and partial deposition of BSA on the analytical area. After switching back to the deionized water, the density of the liquid decreases, causing some increase of the propagation delay, but since at least part of the analytical area is covered with BSA, the average velocity of the acoustic waves traveling at the interface between the liquid and solid remains higher than initial reference, correspondingly causing lower propagation delay readings. Larger shift of the sensor readings after exposure to BSA clearly can be attributed to a higher concentration of the BSA solution. Also, since there are very slight difference between the 3 mg/mL and 1 mg/mL cases, we can conclude that in both cases entire analytical area of the sensor was covered by BSA with only possible difference of the deposition rate, which is indicated by different steepness of the falling slope. As for the 0.1 mg/mL case, it is obvious that sensor readings did not reach the plateau state over the exposure period and there is no detectable difference between the final readings and initial reference. So, for this case we conclude that no detectable amount of BSA was deposited on the analytical area of the sensor.

5. Conclusions

Application of CNN for signal processing of the biosensor was shown to be an improvement in our sensor technology. Particularly, combining of the instant spectra to spectrograms was found to be an effective way for noisy signals classification. For deionized water and saline switching experiment we found a significant decrease of the instrumental noise in the case of the CNN processed sensor readings, which can be quantified as 15 dB improvement of the signal to noise ratio if compared to previously used passband filter signal processing method (75 dB versus 60 dB). Also, it was demonstrated that sensor readings processed by the CNN and additional smoothing filter in the real time perfectly reflect the dynamics of the BSA adsorption on the structure of the biosensor. The shapes of BSA adsorption/desorption curves are comparable to the cases known from earlier works [19]. From recorded readings shown in the Fig. 11 we estimate the ability of the sensor to detect at least three cases of the BSA deposition, i.e. when there is no observable shift of the initial reference value after sensor's exposure to the BSA, corresponding to the 0.1 mg/mL concentration of the BSA solution; also two cases of the shift of the readings, particularly by 6 ns in the case of 0.4 mg/mL concentration of the BSA solution and by 9 ns in the case of 1.0 mg/mL and 3 mg/mL concentrations of the BSA solutions. This gives us a rough estimation of the possible quantification range of the sensor. The cases of 1.0 mg/mL and 3 mg/mL differ only by the rate at which the sensor readings reach plateau state during the BSA exposure and exhibit the same shift after the exposure, so it can be concluded that no more BSA can be deposited within the sensor structure even with an increase of the concentration.

Acknowledgement

This research was supported by the Research, Development and Innovation Fund of Kaunas University of Technology, Lithuania (BioCMUT project grant No. PP32/1802) and in part by the Research Council of Lithuania under the grant No. P-MIP-17-22/S-MIP-17-93 by sharing the CMUT fabrication technology. It was also in part supported by the grant No. 01.2.2-LMT-K-718-02-0012 by paying the salary for dr. Mindaugas Dzikaras, which was involved to test the application of the biosensor. Authors thank Panevėžys mechatronics center (www.panmc.lt) for providing necessary research infrastructure and instrumentation.

References

[1] R. Fogel, J. Limson, A.A. Seshia, Acoustic biosensors, Essays Biochem. 60 (2016) 101–110.
[2] S. Rodriguez-Mozaz, M.P. Marco, M.J.L. de Alda, D. Barceló, Biosensors for environmental applications: Future development trends, Pure Appl. Chem. 76 (2004) 723–752.
[3] E. Sapeliauskas, D. Barauskas, G. Vanagas, D. Virzonis, Surface micromachined CMUTs for liquid phase sensing, 2014 IEEE International Ultrasonics Symposium (Ius), 2014, pp. 2580–2583.
[4] S. Eaimkhong, Label-free biodetection using capacitive micromachined ultrasonic transducers (CMUTs) and its application for cardiovascular disease diagnostics, J. Nanomed. Nanotechnol. 03 (2012).
[5] C. Derec, V. Leroy, D. Kaurin, L. Arbogast, C. Gay, F. Elias, Propagation of a transverse wave on a foam microchannel, EPL (Europhys. Lett.) 112 (2015) 34004.
[6] D. Pelenis, D. Barauskas, E. Sapeliauskas, G. Vanagas, M. Mikolajunas, D. Virzonis, Acoustical streaming in microfluidic CMUT integrated chip controls the biochemical interaction rate, J. Microelectromech. Syst. 26 (2017) 1012–1017.
[7] G. Andria, F. Attivissimo, N. Giaquinto, Digital signal processing techniques for accurate ultrasonic sensor measurement, Measurement 30 (2001) 105–114.
[8] M.J.G. Mølgaard, M. Laustsen, M.H. Jakobsen, T.L. Andresen, E.V. Thomsen, Combined colorimetric and gravimetric CMUT sensor for detection of benzyl methyl ketone, Sens. Actuators, B 275 (2018) 483–489.
[9] G.R. Potty, J.H. Miller, Measurement and modeling of Scholte wave dispersion in coastal waters, 2012, pp. 500–507.
[10] D. Pelenis, A. Dzedzickis, I. Morkvenaite-Vilkonciene, V. Bucinskas, D. Barauskas, G. Vanagas, et al., Non-contact sensing of elastic modulus of the UV cured furniture coatings by the transverse acoustical waves, IEEE Sens. J. 18 (2018) 6527–6532.
[11] B.E. Treeby, J. Jaros, D. Rohrbach, B.T. Cox, Modelling elastic wave propagation using the k-Wave MATLAB Toolbox, 2014 IEEE International Ultrasonics Symposium (Ius), 2014, pp. 146–149.
[12] R. van Vossen, J.O.A. Robertsson, C.H. Chapman, Finite-difference modeling of wave propagation in a fluid–solid configuration, Geophysics 67 (2002) 618–624.
[13] Y. Hoshen, R.J. Weiss, K.W. Wilson, Speech acoustic modeling from raw multichannel waveforms, 2015 IEEE International Conference on Acoustics, Speech, and Signal Processing (Icassp), 2015, pp. 4624–4628.
[14] W. Dai, C. Dai, S.H. Qu, J.C. Li, S. Das, Very deep convolutional neural networks for raw waveforms, Int. Conf. Acoust. Spee, 2017, pp. 421–425.
[15] P. Ghahremani, V. Manohar, D. Povey, S. Khudanpur, Acoustic modelling from the signal domain using CNNs, Interspeech 2016 (2016) 3434–3438.
[16] P. Sonkoly, P. Kozma, Z. Nagy, P. Szolgay, Acoustic wave propagation modeling on 3D CNN-UM architecture, 2006 10th International Workshop on Cellular Neural Networks and Their Applications, 2006, pp. 1–6.
[17] W. Zhang, J. Han, Towards heart sound classification without segmentation using convolutional neural network, Comput. Cardiol. 44 (2017).
[18] H. Akhundi, M. Ghafoori, G.-R. Lashkaripour, Prediction of shear wave velocity using artificial neural network technique, multiple regression and petrophysical data: a case study in Asmari Reservoir (SW Iran), Open J. Geol. (2014) 303–313.
[19] T.N. Sainath, A.-R. Mohamed, B. Kingsbury, B. Ramabhadran, Deep convolutional neural networks for LVCSR, 2013 IEEE International Conference on Acoustics, Speech and Signal Processing, 2013, pp. 8614–8618.
[20] D. Barauskas, G. Vanagas, D. Virzonis, A. Ramanaviciene, A. Makaraviciute, A. Ramanavicius, Application of CMUT as immunosensor, IEEE Int. Ultra Sym. (2013) 1708–1711.
[21] M. Goto, H. Yatsuda, J. Kondoh, Simulation for viscoelastic effects of SH-SAW biosensor, 2014, pp. 2051–2054.
[22] J. Mclean, F.L. Degertekin, Directional Scholte wave generation and detection using interdigital capacitive micromachined ultrasonic transducers, IEEE Trans. Ultras. Freq. Contr. 51 (2004) 756–764.